Motion Primitive Approach to Spacecraft Trajectory Design in the Neptune-Triton System

Giuliana E. Miceli* and Natasha Bosanac†
University of Colorado Boulder, Boulder, Colorado, 80303

Jeffrey R. Stuart‡ and Farah Alibay§
Jet Propulsion Laboratory, California Institute of Technology, Pasadena, California, 91109

The identification of the Neptunian system as a high-priority target for future missions motivates the design of trajectories that can deliver a spacecraft from a high-energy interplanetary arrival condition to scientifically meaningful locations within a chaotic dynamical environment. This paper addresses this challenging task by using a motion primitive approach to spacecraft trajectory design. First, a target mission orbit is selected as a 3:4 resonant orbit in the Neptune-Triton system. A motion primitive library is then constructed by using clustering to summarize arcs along selected fundamental solutions in the circular restricted three-body problem. A graph that captures their potential connectivity is searched to form motion primitive sequences. Selected sequences are refined and corrected to produce geometrically distinct spacecraft trajectories with flight times as low as 12.60 days and total impulsive maneuver requirements as low as 1.64 km/s.

I. Introduction

The 2023 NASA Decadal Survey identifies Neptune as a high-priority target for future missions with the potential to supply insight into the characteristics, formation, and evolution of our solar system [1]. Mission concepts to visit this icy giant have been formulated for flybys, orbiters, and probes [2–4]. Across the variety of mission architectures, a common challenge emerges: designing trajectories for the spacecraft to visit scientifically meaningful locations in the complex dynamical environment of the Neptunian system after the spacecraft has completed its interplanetary transfer. In this scenario, trajectory design is a particularly challenging task due to the high energy arrival conditions, limited maneuverability, complexity of a multi-body gravitational system, and constraints that are derived from hardware parameters or operational requirements.

Several researchers have designed trajectories for spacecraft within various dynamical models of the Neptunian system. One common approach involves using patched conics to approximate the gravitational environment of a multi-body system as a sequence of two-body problems [5]. This approach has been used in mission concept studies presented by Marley et al. [6] and Masters [3], where multiple Triton flybys are used to study the Neptunian moon. However, trajectories that exist in a multi-body system but are designed using a patched-conics approach can sometimes result in the investigation of a limited portion of the solution space with sub-optimal combinations of propellant mass usage and flight. More complex approaches include approximating a multi-body system by focusing on the gravitational influence of the planet and a single moon and using the circular restricted three-body problem (CR3BP). For instance, Melman et al. computed a transfer for a spacecraft from a Neptune-centered orbit to a circular near-polar orbit around Triton in the CR3BP [7]. Increasing the complexity of the dynamical model could lead to the use of the patched CR3BP, the bicircular four-body problem, or an ephemeris model. In these cases, the time-dependence, high-dimensionality, or absence of fundamental solutions may render trajectory design an even more challenging problem.

The state of the art for spacecraft trajectory design in a multi-body system currently involves a manual process that leverages dynamical systems techniques to explore the solution space and then construct an initial guess [8]. First, where appropriate, the dynamical environment may be approximated by a low-fidelity model such as the CR3BP.

*Graduate Research Assistant, Colorado Center for Astrodynamics Research, Smead Department of Aerospace Engineering Sciences, giuliana.miceli@colorado.edu

†Assistant Professor, Colorado Center for Astrodynamics Research, Smead Department of Aerospace Engineering Sciences, natasha.bosanac@colorado.edu, AIAA Senior Member.

‡GNC Engineer, Mission Design and Navigation, Jet Propulsion Laboratory, California Institute of Technology, AIAA Senior Member.

§System Engineer, Flight System Systems Engineering, Jet Propulsion Laboratory, California Institute of Technology, AIAA Member.

Then, fundamental solutions such as equilibrium points, periodic orbits, quasi-periodic orbits, and hyperbolic invariant manifolds are computed. Arcs along these solutions, or even more general arcs, are then assembled in a sequence, along with maneuvers, to form an initial guess for a trajectory. An initial guess is then corrected in a higher-fidelity model and optimization may be applied to lower the total maneuver magnitude. However, initial guess construction and design space exploration in this approach are challenging and time-consuming tasks, particularly for spatial motion at high energies and with constraints.

To address the challenges of trajectory design within a multi-body gravitational system, we leverage a motion primitive approach that has recently been developed by Smith and Bosanac [9, 10]. Most commonly used in robotics, motion primitives have been described by Wolek and Woolsey as fundamental building blocks of motion [11]. These motion primitives have typically been extracted using manual labeling, clustering, or basis function approximations [12–15]. Then, a continuous-time path-planning problem may be reformulated as a discrete graph search problem. For instance, Frazzoli as well as Majumdar and Tedrake have constructed graphs by defining the nodes as motion primitives and directed edges connecting selected nodes [12, 16]. Graph search algorithms may then be used to construct sequences of motion primitives that form a complex trajectory. This approach has been successfully used in a variety of problems, from describing and planning motion for humans or robots performing simple movement tasks [17–19] to path planning for autonomous vehicles in the air and on land [12, 16–19]. Inspired by their use in these applications, Smith and Bosanac developed a motion primitive approach to spacecraft trajectory design in a multi-body system [10]. They demonstrated this approach by designing spacecraft transfers with impulsive maneuvers between selected libration points orbits in the Earth-Moon CR3BP.

This paper leverages and builds upon the motion primitive approach developed by Smith and Bosanac to design planar spacecraft trajectories from a high-energy interplanetary arrival condition to a periodic orbit in the Neptune-Triton CR3BP with impulsive maneuvers. First, a target mission orbit is selected as a planar 3:4 resonant orbit to support a notional scientific goal of performing magnetometric induction measurements at Triton. This orbit meets the requirements presented by Cochrane et al. that a spacecraft must perform multiple flybys of Triton at altitudes between 300 and 350 km at equally spaced locations along Triton's orbit [20]. Next, a motion primitive library is constructed to supply a subset of building blocks of trajectories that connect the specified boundary conditions. These motion primitives are generated by using clustering to summarize arcs along selected planar periodic orbit families and their associated hyperbolic invariant manifolds in the Neptune-Triton CR3BP. A graph is then constructed to reflect the potential connectivity of these motion primitives and the selected boundary conditions. This graph is searched to generate distinct primitive sequences that are refined to construct initial guesses. These initial guesses are corrected using collocation and multi-objective optimization to produce nearby continuous paths in the Neptune-Triton CR3BP, with continuation used to gradually reduce the maneuver requirements. The result is a few geometrically distinct spacecraft trajectories that exist in the CR3BP and reach the selected target orbit after a high-energy arrival into the Neptunian system. These trajectories possess flight times as low as 12.60 days and total maneuver requirements as low as 1.64 km/s.

II. Background

A. Dynamical Model

In this paper, the motion of a spacecraft in the Neptunian system is approximated by the Neptune-Triton CR3BP. In this dynamical model, the spacecraft is assumed to possess a negligible mass relative to two primary bodies with masses M_1 and M_2 [21]. Although the Neptunian system includes 14 moons, Triton is the most massive moon by approximately two orders of magnitude [22]. Accordingly, the two primary bodies of the CR3BP are selected as Neptune and Triton. These bodies are also assumed to follow circular orbits about their barycenter [21]; this assumption is reasonable because their average orbital eccentricity is 0.000016 [22].

The equations of motion governing a spacecraft in the Neptune-Triton CR3BP are written in the Neptune-Triton rotating frame using nondimensional quantities [21]. The Neptune-Triton rotating frame uses the system barycenter as the origin and axes $\hat{\boldsymbol{x}}, \hat{\boldsymbol{y}}, \hat{\boldsymbol{z}}$: $\hat{\boldsymbol{x}}$ is directed from Neptune to Triton, $\hat{\boldsymbol{z}}$ is directed along the orbital angular momentum vector of the primary bodies, and $\hat{\boldsymbol{y}}$ completes the right-handed triad [21]. In the CR3BP, it is also common to nondimensionalize length, time, and mass quantities by the characteristic quantities l^*, m^*, and t^* [21]: $m^* \approx 1.024569 \times 10^{26}$ kg is the sum of the masses of Neptune and Triton; $l^* = 354,760$ km is set equal to the average distance between Neptune and Triton, and $t^* \approx 8.081353 \times 10^4$ s sets the mean motion of the primary system to unity [23]. In this frame, the nondimensional state of the spacecraft is defined as $\boldsymbol{x} = [x, y, z, \dot{x}, \dot{y}, \dot{z}]^T$. Then, the nondimensional equations of motion for the spacecraft in the Neptune-Triton rotating frame are written as

$$\ddot{x} = 2\dot{y} + \frac{\partial U^*}{\partial x}, \quad \ddot{y} = -2\dot{x} + \frac{\partial U^*}{\partial y}, \quad \ddot{z} = \frac{\partial U^*}{\partial z} \tag{1}$$

where

$$U^* = \frac{1}{2}(x^2 + y^2) + \frac{(1-\mu)}{r_1} + \frac{\mu}{r_2} \tag{2}$$

$$r_1 = \sqrt{(x+\mu)^2 + y^2 + z^2} \quad \text{and} \quad r_2 = \sqrt{(x-1+\mu)^2 + y^2 + z^2} \tag{3}$$

In these equations, the mass ratio of the Neptune-Triton system is $\mu = M_2/(M_1 + M_2) \approx 0.00020895$. The only integral of motion of this autonomous dynamical system is the Jacobi constant, defined as $C_J = 2U^* - \dot{x}^2 - \dot{y}^2 - \dot{z}^2$ [21]. The Jacobi constant is an energy-like quantity that is commonly used to derive heuristics during the trajectory design process.

B. Fundamental Solutions

The solution space of the CR3BP includes fundamental solutions such as equilibrium points, families of periodic and quasi-periodic orbits, and their hyperbolic invariant manifolds. In the CR3BP, there are five equilibrium points in the rotating frame: the collinear points L_1, L_2, and L_3, and the triangular points L_4 and L_5. Periodic orbits are trajectories that repeat their motion in the rotating frame after a minimal time which is labeled the orbital period. These orbits exist throughout the system in continuous, one-parameter families. Quasi-periodic orbits correspond to bounded motions that trace out the surface of a torus near a stable periodic orbit. Unstable periodic orbits, however, indicate the existence of stable and unstable manifolds that are defined as the collection of states that approach a periodic or quasi-periodic orbit as time tends to $+\infty$ or $-\infty$, respectively. Arcs along these natural solutions are often used to construct initial guesses for a spacecraft trajectory because they govern natural motion within a multi-body system.

This paper uses planar families of Lyapunov and resonant orbits, as well as their hyperbolic invariant manifolds, in this preliminary demonstration of a motion primitive approach to transfer design in the Neptune-Triton system. Planar periodic orbits emanating from the collinear equilibrium points, L_1 to L_3, are labeled Lyapunov orbits. Initial guesses for a single periodic orbit within these families are typically generated from a linear stability analysis of the nearby equilibrium point [21]. Along the Lyapunov orbit families, periodic orbits can extend far from the equilibrium points to even include some close passages to the primaries. Resonant orbits, however, orbit about one or both primaries and can visit various regions of a system. The definition of a resonant orbit in the CR3BP is derived from its original definition in the two-body problem. Specifically, a spacecraft that is located along a $p:q$ resonant orbit completes p revolutions around the larger primary body (i.e., Neptune) in approximately the time that the smaller primary body (i.e., Triton) completes q revolutions in the inertial frame [24]. When $p > q$, the orbit is labeled an interior resonance and primarily revolves around the larger primary. Alternatively, when $p < q$, the orbit is labeled an exterior resonance with motion predominantly in the exterior region of the system. Finally, a prograde (or retrograde) resonant orbit possesses an orbital angular momentum vector with respect to Neptune that is predominantly aligned with the positive (or negative) third axis in the inertial frame.

An initial guess for a $p:q$ resonant orbit is typically generated using a resonant elliptical orbit in the two-body problem [24, 25]; for a small value of μ, this approximation tends to supply a suitable initial guess. First, the semi-major axis of the elliptical orbit followed by the spacecraft in the two-body problem is calculated as $a = (q/p)^{2/3} a_T$, where a_T is the semi-major axis of Triton's orbit. However, the eccentricity of an ellipse in the inertial frame that leads to a good initial guess for a periodic orbit in the CR3BP is not yet known; thus, the eccentricity e is a variable. Next, an initial state is defined in the inertial frame at periapsis or apoapsis to produce prograde or retrograde motion along an ellipse with eccentricity e. The selected initial state is nondimensionalized and transformed to the Neptune-Triton rotating frame. This initial state is then propagated in the CR3BP for a nondimensional orbit period $T_{pq} = qT_2$ in the rotating frame. This process is repeated as the eccentricity is varied and the path with the smallest difference between the initial and final state supplies the initial guess for a $p:q$ resonant orbit in the rotating frame of the Neptune-Triton CR3BP.

Once an initial guess is generated, a single periodic orbit is numerically generated using a multiple-shooting approach to differential corrections. First, the initial guess is discretized into several arcs with an equal integration time. Then, the initial, nondimensional state along those arcs in the rotating frame and the integration time form the free variable vector. This free variable vector is iteratively updated using Newton's method with the goal of satisfying the following constraints: continuity between neighboring arcs and periodicity. These free variables are updated until the norm of the associated constraint vector equals zero to within a tolerance of 10^{-10} or until a maximum number of iterations.

Using a single periodic orbit, additional members along the associated one-parameter family are computed using pseudo-arclength continuation. Specifically, an initial guess for a nearby member of the family is generated by perturbing the free variable vector of the known periodic orbit in the direction of the local tangent vector along the family. This new initial guess is corrected to satisfy the periodicity and continuity constraints. The new periodic orbit is also constrained to possess a free variable vector with a fixed-length projection onto the local tangent to the family at the previously computed orbit. The desired length of this projection is adaptively varied when too many iterations are required to correct a periodic orbit or the norm of the constraint vector diverges. This process is repeated until reaching any specified termination conditions such as intersecting one of the primaries or reaching a maximum number of iterations during corrections before the norm of the constraint vector falls below the selected tolerance.

A linear estimate of the stability of a periodic orbit is computed from the eigenvalues of its monodromy matrix. The six eigenvalues exist in reciprocal pairs; two non-trivial pairs indicate the qualitative behavior of motion near the periodic orbit. The sum of each nontrivial pair of eigenvalues defines the stability indices s_1 and s_2; these quantities are an integer multiple of the stability indices defined by Howell in 1984 [26]. If one of the stability indices possesses a value in the range $[2, -2]$, i.e., the eigenvalues lie along the unit circle in the complex plane, bounded trajectories exist in the vicinity of the periodic orbit. Otherwise, when one of s_1 or s_2 possesses a magnitude greater than 2, the periodic orbit admits stable and unstable invariant manifolds.

The stable or unstable manifolds of a periodic orbit are typically computed numerically by generating two half-manifolds [8]. First, a state $\boldsymbol{x}_{PO}$ is sampled along an unstable periodic orbit, and a perturbation is applied parallel or anti-parallel to a stable (or unstable) eigenvector of the associated monodromy matrix [8]. This state is propagated backward (or forward) in time for a selected time interval, supplying a single trajectory along the associated stable (or unstable) half-manifold. This process is repeated for more states along the periodic orbit and for perturbations parallel or anti-parallel to the associated eigenvector until a discrete representation of each half-manifold is generated.

C. Numerically Correcting Trajectories

Collocation is used in this paper to correct an initial guess to produce a continuous trajectory due to its robustness. Specifically, the trajectory corrections problem is reframed as the computation of a sequence of polynomials that approximate the continuous path and satisfy the system dynamics at selected points [27–29]. This problem is mathematically defined using a free variable and constraint vector formulation. The formulation presented in this paper is based upon the odd-degree collocation scheme with hybrid mesh refinement presented by Grebow and Pavlak [30]; this approach was also employed by Smith and Bosanac to correct primitive-based initial guesses [31].

The collocation process begins by using the initial guess to define a mesh of nodes. First, the initial guess is discretized into N segments and the i-th segment is further discretized into m_i arcs; the trajectory designer manually selects initial values of N and m_i. Then, n nodes are distributed along each arc; the number and location of these nodes are explained in the next paragraph. The k-th node along the j-th arc within the i-th segment corresponds to a state, $\boldsymbol{x}^i_{j,k}$, and time elapsed from the first node along the entire trajectory, $t^i_{j,k}$. At a general time t along this same arc, a nondimensional elapsed time is defined from the first node as $\tau = 2((t - t^i_{j,1})/\Delta t^i_j) - 1 \in [-1, 1]$ where Δt^i_j is the integration time of the arc.

Collocation nodes are distributed along each arc based on the order of the polynomials used to approximate the arc and a selected node spacing strategy. In this paper, 7-th order polynomials are used due to their previous successful application to several trajectory corrections and optimization in multi-body systems [27, 28, 30–34]. Accordingly, $n = 7$ collocation nodes are placed along each arc. Then, a Legendre-Gauss-Lobatto (LGL) node spacing strategy is employed to place these 7 nodes at the boundaries of each arc as well as the values of τ that are equal to the roots of the derivative of the $(n - 1)$-th order Legendre polynomial [27, 30, 35].

Along the j-th arc within the i-th segment, there are two types of collocation nodes: free nodes and defect nodes. Free nodes are used to construct the polynomial approximation of each arc and correspond to the odd-numbered collocation odes; these free nodes are described by their state vector $\boldsymbol{x}^i_{j,k}$ and time $\boldsymbol{t}^i_{j,k}$ for $k = 1, 3, 5, 7$. Defect nodes, however, are used to compare the polynomial representation of the arc to the system dynamics; these defect nodes are described by the value of the polynomial $\boldsymbol{p}^i_j(\tau_k)$ at the associated time $\boldsymbol{t}^i_{j,k}$ for $k = 2, 4, 6$.

A free variable vector that describes the mesh of nodes is formulated to include the states at all the free nodes and the propagation time along each arc. For the i-th segment, these variables are

$$\boldsymbol{V}_i = \left[\begin{bmatrix} \boldsymbol{x}^i_{1,1} \\ \boldsymbol{x}^i_{1,3} \\ \boldsymbol{x}^i_{1,5} \end{bmatrix}^T \quad \begin{bmatrix} \boldsymbol{x}^i_{2,1} \\ \boldsymbol{x}^i_{2,3} \\ \boldsymbol{x}^i_{2,5} \end{bmatrix}^T \quad \dots \quad \begin{bmatrix} \boldsymbol{x}^i_{m_i-1,1} \\ \boldsymbol{x}^i_{m_i-1,3} \\ \boldsymbol{x}^i_{m_i-1,5} \end{bmatrix}^T \quad \dots \quad \begin{bmatrix} \boldsymbol{x}^i_{m_i,1} \\ \boldsymbol{x}^i_{m_i,3} \\ \boldsymbol{x}^i_{m_i,5} \\ \boldsymbol{x}^i_{m_i,7} \end{bmatrix}^T \quad \begin{bmatrix} \Delta t^i_{1,i} \\ \Delta t^i_{2,i} \\ \vdots \\ \Delta t^i_{m_i,i} \end{bmatrix}^T \right] \tag{4}$$

To implicitly enforce continuity between arcs along the same segment, the final node along the j-th arc is assumed to coincide with the initial node along the $j+1$-th arc for $j \in [1, m_i - 1]$. Thus, $\boldsymbol{x}^i_{j,n}$ is not included in the free variable vector for $j \in [1, m_i - 1]$. Across all segments of the trajectory, the complete free variable vector is then defined as

$$\boldsymbol{V} = \left[\boldsymbol{V}_1, \boldsymbol{V}_2, \dots, \boldsymbol{V}_N \right]^T \tag{5}$$

to include a total of $((3n-2)\sum_{i=1}^{N} m_i + 6N)$ variables.

The constraint vector is defined to enforce continuity between segments and ensure that the system dynamics are satisfied at the defect nodes. The continuity constraint between the end of the i-th segment and the beginning of the $i+1$-th segment is expressed as:

$$\boldsymbol{F}^i_c = \begin{cases} (\boldsymbol{x}^{i+1}_{1,1} - \boldsymbol{x}^i_{m_i,n})^T \text{ if natural motion} \\ (\boldsymbol{r}^{i+1}_{1,1} - \boldsymbol{r}^i_{m_i,n})^T \text{ if impulsive maneuver applied} \end{cases} \tag{6}$$

for $i < N$. Then, the defect constraints are formulated to ensure that the derivative of the polynomial approximation of each arc equals the state derivative computed using the system dynamics at the defect nodes. For the j-th arc along the i-th segment, the defect constraint is written as

$$\boldsymbol{F}^i_{d,j} = \begin{bmatrix} (\dot{\boldsymbol{p}}^i_{j,2}(\tau_2) - \dot{\boldsymbol{x}}^i_{j,2})w_2 \\ (\dot{\boldsymbol{p}}^i_{j,4}(\tau_4) - \dot{\boldsymbol{x}}^i_{j,4})w_4 \\ (\dot{\boldsymbol{p}}^i_{j,6}(\tau_6) - \dot{\boldsymbol{x}}^i_{j,6})w_6 \end{bmatrix}^T \tag{7}$$

where w_k is the LGL weight associated with the k-th collocation node and $\dot{\boldsymbol{p}}$ is the derivative of the polynomial along the arc with respect to normalized time τ. In this expression, $\dot{\boldsymbol{x}}$ is the normalized time derivative of the state vector $\boldsymbol{x}^i_{j,k}$ that is calculated as

$$\dot{\boldsymbol{x}}^i_{j,k} = \frac{\Delta t^i_j}{2} \boldsymbol{g}(\boldsymbol{x}^i_{j,k}) \tag{8}$$

where $\boldsymbol{g} = [\dot{x}, \dot{y}, \dot{z}, \ddot{x}, \ddot{y}, \ddot{z}]$. For all m_i arcs along the i-th segment, the defect constraint vector is

$$\boldsymbol{F}^i_d = \left[\boldsymbol{F}^i_{d,1}, \boldsymbol{F}^i_{d,2}, \dots, \boldsymbol{F}^i_{d,m_i} \right] \tag{9}$$

The continuity constraint vectors and the defect constraint are then concatenated to produce the complete constraint vector, equal to

$$\boldsymbol{F}(\boldsymbol{V}) = \left[\boldsymbol{F}^1_c, \boldsymbol{F}^2_c, \dots, \boldsymbol{F}^{N-1}_c, \boldsymbol{F}^1_d, \boldsymbol{F}^2_d, \dots, \boldsymbol{F}^N_d \right]^T \tag{10}$$

Newton's method is then employed to iteratively update the free variable vector $\boldsymbol{V}$ until the norm of this constraint vector is equal to zero to within a tolerance of 10^{-12}.

A mesh refinement process is used during the corrections process to improve the accuracy of the solution [31]. When correcting the free nodes and integration times to satisfy the constraint vector, sometimes the defect constraints along each arc can be met even if the polynomial does not accurately approximate the system dynamics. The mesh refinement allows the replacement of nodes along the most sensitive regions of the trajectory such that the error along the segments is redistributed equally along the arcs of the solution [33]. This paper uses the hybrid mesh refinement presented by Grebow and Pavlak and Carl de Boor's method for error redistribution [30, 36, 37]; this same approach was used by Smith and Bosanac when correcting primitive-based initial guesses [31].

The first step of mesh refinement is to redistribute the error in the polynomial approximation along the mesh. In this step, Carl de Boor's method is used to adjust the location of the nodes at the boundaries of each arc and, therefore, the integration time along each arc; the total number of arcs does not change. Once the boundary nodes of each arc have been updated, the polynomials computed from the previous mesh are used to place the LGL nodes along each arc in the new mesh. This error distribution is repeated until: the maximum error difference along the current solution between any two arcs is $\leq 10^{-5}$; the maximum error difference along the current solution changed by $\leq 10\%$ from the previous iteration; or a maximum number of iterations, selected in this paper as 5, is exceeded. The values used to specify these termination conditions are the same as those used by Smith and Bosanac but may be adjusted as needed [31].

Next, Control with Explicit Propagation (CEP) is used to iteratively merge or split arcs to balance reducing the dimension of the corrections problem with reducing the error along each arc [30, 33]. First, the state $\boldsymbol{x}^i_{j,1}$ at the first node along the j-th arc within the i-th segment is propagated forward in time for $\Delta t^i_j + \Delta t^i_{j+1}$. If the magnitude of the error between this propagated state and the state $\boldsymbol{x}^i_{j+1,n}$ at the final node of the $j+1$-th arc is below a tolerance of 10^{-13}, these two arcs are merged into a single arc. Next, the state $\boldsymbol{x}^i_{j,1}$ at the first node along the j-th arc within the i-th segment is propagated forward in time for Δt^i_j. If the error between this propagated state and the state $\boldsymbol{x}^i_{j,n}$ is above a tolerance of 10^{-12}, the arc is split into two arcs with the same integration time. For either split or merged arcs, the collocation nodes are recomputed between the updated boundary nodes using the polynomials from the previous mesh. With this new mesh, the correction process is implemented again to produce a new continuous trajectory. This iterative process continues until there are no more arcs to merge or split or a maximum of 10 iterations is exceeded [31].

III. Technical Approach

The motion primitive approach to trajectory design is summarized in this section. This process consists of the following steps:

1) Generate a library of motion primitives that summarizes natural arcs along selected families of periodic orbits and their stable/unstable manifolds.
2) Formulate a motion primitive graph that reflects their potential for connectivity.
3) Search the motion primitive graph to produce a sequence of motion primitives that is refined to produce an initial guess for a trajectory.
4) Correct the initial guess to produce a continuous trajectory with impulsive maneuvers.

Because this approach closely follows the approach originally developed by Smith and Bosanac, only a brief summary is presented in this paper. For further details, the reader is referred to Smith and Bosanac 2022 [31]. However, there are some improvements to the process for generating motion primitives and searching the graph to produce a primitive sequence; these updates are described in detail.

A. Step 1: Generate Motion Primitives

A library of motion primitives is generated to discretely summarize arcs along continuous families of periodic orbits and/or their hyperbolic invariant manifolds. The general process for motion primitive extraction used in this paper follows the approach presented by Smith and Bosanac [9], with some modifications to improve the quality of the primitives in this application. First, arcs along each of these families of solutions are sampled and described using finite-dimensional feature vectors that encode characteristics of interest. In this paper, a new curvature-based sampling scheme and position-based feature vector description are presented to more generally summarize the geometry of arcs that exist in various regions of the Neptune-Triton system. Then, following the approach presented by Smith and Bosanac, consensus clustering is used to extract groups of similar feature vectors. The associated groups of trajectories are then summarized by a single member, labeled the motion primitive. The resulting library of motion primitives produces a discrete summary of a subset of the continuous solution space.

Each trajectory that is sampled from a periodic orbit family or along a hyperbolic invariant manifold is discretized into a sequence of states. This approach produces a finite-dimensional, time-series representation of a continuous trajectory. To limit the number of states sampled along the trajectory, the goal is to place these samples at the most meaningful locations that capture its shape. In the field of computer graphics, this task is typically labeled shape interrogation and one approach is to use the concept of curvature to identify the most geometrically meaningful locations along a shape or curve [38]. Recently in astrodynamics, Bosanac has used this idea to summarize general trajectories by evenly sampling a fixed number of states in the integral of the curvature along a trajectory prior to using clustering to produce a set of geometrically distinct groups [39]. Spear and Bosanac have also used maxima in the curvature as a mechanism for determining the number of states to sample along a trajectory prior to clustering [40]. Inspired by these applications, each trajectory in this paper is sampled at extrema in the curvature.

Derived from differential geometry, the value of the curvature at a location along a trajectory captures the deviation from a straight line. Mathematically, the curvature is calculated at a single state along a trajectory as [38]

$$\kappa(\boldsymbol{x}) = \frac{\sqrt{(\dot{x}\ddot{y} - \dot{y}\ddot{x})^2 + (\dot{z}\ddot{x} - \dot{x}\ddot{z})^2 + (\dot{y}\ddot{z} - \ddot{y}\dot{z})^2}}{(\dot{x} + \dot{y} + \dot{z})^{3/2}} \tag{11}$$

At an extremum in the curvature, the following condition must be satisfied:

$$\begin{aligned} \dot{\kappa}(\boldsymbol{x}) = 0 = & \frac{2(\dddot{y}\dot{x} - \dddot{x}\dot{y})(\dot{x}\ddot{y} - \ddot{x}\dot{y}) + 2(\dddot{x}\dot{z} - \dddot{z}\dot{x})(\dot{z}\ddot{x} - \ddot{z}\dot{x}) + 2(\dddot{z}\dot{y} - \dddot{y}\dot{z})(\dot{y}\ddot{z} - \ddot{y}\dot{z})}{2(\dot{x}^2 + \dot{y}^2 + \dot{z}^2)^{3/2}\sqrt{(\dot{x}\ddot{y} - \dot{y}\ddot{x})^2 + (\dot{z}\ddot{x} - \dot{x}\ddot{z})^2 + (\dot{y}\ddot{z} - \ddot{y}\dot{z})^2}} \\ & - \frac{3(2\dot{x}\ddot{x} + 2\dot{y}\ddot{y} + 2\dot{z}\ddot{z}))\sqrt{(\dot{x}\ddot{y} - \dot{y}\ddot{x})^2 + (\dot{z}\ddot{x} - \dot{x}\ddot{z})^2 + (\dot{y}\ddot{z} - \ddot{y}\dot{z})^2}}{2(\dot{x}^2 + \dot{y}^2 + \dot{z}^2)^{5/2}} \end{aligned} \tag{12}$$

where

$$\dddot{x} = 2\ddot{y} + \dot{x} - \frac{(1-\mu)\dot{x}r_1^3 - (1-\mu)(x+\mu)\dot{r}_1^3}{r_1^6} - \frac{\mu\dot{x}r_2^3 - \mu(x-1+\mu)\dot{r}_2^3}{r_2^6} \tag{13}$$

$$\dddot{y} = -2\ddot{x} + \dot{y} - \frac{(1-\mu)\dot{y}r_1^3 - (1-\mu)y\dot{r}_1^3}{r_1^6} - \frac{\mu\dot{y}r_2^3 - \mu y\dot{r}_2^3}{r_2^6} \tag{14}$$

$$\dddot{z} = -\frac{(1-\mu)\dot{z}r_1^3 - (1-\mu)z\dot{r}_1^3}{r_1^6} - \frac{\mu\dot{z}r_2^3 - \mu z\dot{r}_2^3}{r_2^6} \tag{15}$$

Maxima in the curvature occur at the most significant changes in the shape including, for instance, near the traditional periapsis or apoapsis locations, measured relative to one of the two primaries. However, the use of a maximum in the curvature negates the need to specify the most suitable reference primary for calculating these apses as a trajectory passes through distinct regions of a system. The maxima in the curvature also occur at locations where the trajectory may revolve around other reference points. Minima, however, occur at locations where the shape changes the least and can offer a mechanism to distribute additional samples between some maxima. Together, the states sampled at the extrema in curvature capture the geometry of a trajectory. However, as the trajectories along a single family of solutions evolve, there may be a distinct number of extrema and, therefore, sampled states.

The sampled states are used to form a finite-dimensional description of each trajectory. The result is a feature vector that should capture the characteristics of interest when clustering. In this paper, the goal is to use clustering to extract groups of trajectories with a similar geometry in the configuration space. Thus, the feature vector used to describe the i-th trajectory, discretized into a sequence of states $\boldsymbol{x}_{i,1}, \boldsymbol{x}_{i,2}, ..., \boldsymbol{x}_{i,n}$, is defined in this paper as

$$\boldsymbol{f}_i = \left[\tilde{x}_{i,1}, \tilde{y}_{i,1}, \tilde{z}_{i,1}, \tilde{x}_{i,2}, \tilde{y}_{i,2}, \tilde{z}_{i,2}, \ldots, \tilde{x}_{i,n}, \tilde{y}_{i,n}, \tilde{z}_{i,n}\right] \tag{16}$$

where n is the total number of extrema in the curvature along the trajectory and the tilde indicates normalization within the range of $[-1, 1]$ using the global maximum distance of a sampled state relative to a specified reference point among all trajectories within the dataset [10]. This feature vector is used to describe both periodic orbits and arcs along hyperbolic invariant manifolds. For datasets where there is a variable number of states sampled along the trajectories, this feature vector is augmented by zeros to produce a fixed-length feature vector across the entire dataset.

The feature vectors within each dataset are clustered using Weighted Evidence Accumulation Clustering (WEAC) to produce groupings of geometrically similar trajectories within the configuration space. WEAC is a form of consensus clustering that uses evidence from multiple individual clustering results, each generated using distinct parameters and/or algorithms, to construct a single clustering result. In this paper, multiple clustering results are generated by applying each of k-means and agglomerative clustering with Ward linkage to the feature vectors generated from a single family of solutions. Each algorithm is used to generate multiple clustering results with distinct input parameters: for the selected clustering algorithms, the number of clusters is varied between 3 and 11. Using this information as input, WEAC begins by calculating a co-association matrix for each clustering result to reflect whether members of the dataset are located in the same cluster. For each clustering result, a weight is also computed as a function of a normalized crowd agreement index that captures the average similarity to the other clustering results. The co-association matrices for each clustering result are then weighted and summed to produce a weighted ensemble co-association matrix that serves as a similarity matrix for a desired clustering algorithm to produce the consensus clustering result. In this paper, agglomerative clustering is used with average linkage to generate the final clusters. More details about this clustering process appear in Smith and Bosanac [9].

Each motion primitive is stored in a library along with several exemplars from the associated cluster. The motion primitive is extracted as the cluster medoid, i.e., the member of the cluster that has the smallest difference to all the other members [41]. These exemplars are additional members of the cluster that resemble the primitive and span the associated region of the phase space; these exemplars are useful for constructing the motion primitive graph and improve the quality of each initial guess. For the i-th cluster, the set of exemplars is labeled as R_i [9]. These exemplars are selected by further partitioning the cluster into k subclusters using the k-means clustering algorithm, where the value of k is specified by the user. This step produces k evenly sized subclusters and their medoids supply the exemplars stored in R_i [9]. If a cluster has fewer than k members, all the trajectories are labeled as exemplars. In either case, the set of exemplars is also augmented to include trajectories that lie at the extrema of selected characteristics: these are the Jacobi constant for periodic orbit families, and total propagation time along an arc for hyperbolic invariant manifolds.

B. Step 2: Create A Motion Primitive Graph

A motion primitive graph is constructed to discretely summarize a segment of the solution space. A graph is a data structure composed of nodes and edges used to model properties and relationships within a network of objects [42, 43]. When motion primitives have been used in other disciplines for path-planning, a motion primitive graph is typically constructed. In one common approach, the primitives are assigned as the nodes whereas the edges reflect their potential for sequential composability [12, 16]. Following a similar approach, Smith and Bosanac constructed a motion primitive graph in two steps to enable input from a trajectory designer and, in some cases, to reduce the size of the graph [31]. First, they construct subgraphs that capture the potential connectivity between primitives derived from the same family of solutions. Then, they construct a high-level itinerary graph to determine which subgraphs should be connected. This subsection presents a brief overview of this procedure which is also used in this paper; more details can be found in Smith and Bosanac 2023 [31].

The potential for sequential composability is calculated between pairs of primitives and their associated exemplars to reflect the potential for an ordered sequence of one arc from each pair to produce a nearby continuous trajectory. Consider the following ordered sequence of arcs: arc i is followed by arc j. Their potential for sequential composability $q_{i,j}$ is calculated as

$$q_{i,j} = \alpha_{pos} \Delta r_{i,j} + \alpha_{vel} \Delta v_{i,j} \tag{17}$$

where $\Delta r_{i,j}$ and $\Delta v_{i,j}$ are the differences in position and velocity between one state on the i-th arc and one state on the j-th arc. To evaluate these state differences, each of the two arcs is sampled at a set of n_s states, evenly distributed along the arclength of the arc. The states used to calculate the position and velocity differences in Equation 17 are identified using one of the following four approaches:

1) the final state of arc i and the initial state of arc j
2) the closest state along arc i to the initial state of arc j, minimizing the value of $q_{i,j}$
3) the closest state along arc j to the final state of arc i, minimizing the value of $q_{i,j}$
4) the closest states along arcs i and j that minimize the value of $q_{i,j}$

The trajectory designer may select either of these approaches to calculate Δr and Δv as well as the scaling weights α_{pos} and α_{vel}. When the exemplars are included in the calculation of the sequential composability of two primitives, the minimum value of $q_{i,j}$ between any two arcs in each set is used.

For selected families of periodic orbits or hyperbolic invariant manifolds, identified by the trajectory designer, individual subgraphs are constructed. This subgraph may either be internally connected, indicating the potential to sequentially compose two primitives from the same family, or internally disconnected, indicating that only one primitive can be selected from that subgraph. If the set is internally connected, each node is connected via weighted and directed intra-subgraph edges to its k-nearest neighbors, identified via the k lowest values of their potential for sequential composability; this value of k is specified by the trajectory designer.

A high-level itinerary graph defines the connection between and order of the subgraphs within the full motion primitive graph. This itinerary graph can be constructed to reflect the trajectory designer's experience or lack thereof in a specific scenario. First, the initial and target arcs or states supply nodes in this itinerary graph with only uni-directional edges. Then, subgraphs that summarize arcs along specific families are selected by the designer. The connection between these subgraphs must be defined, including which pairs of subgraphs can be connected and whether those connections are uni- or bi-directional.

To complete the motion primitive graph, inter-subgraph edges are constructed between members of connected subgraphs. For two subgraphs connected by a uni-directional edge in the itinerary graph, edges are added between each primitive in the first subgraph to its k-nearest neighbors in the second subgraph. If the subgraphs are connected by a bi-directional edge, this process is performed for each ordered combination of the subgraphs. Similar to the intra-subgraph edges, these inter-subgraph edges are also weighted by their associated value of the sequential composability q.

C. Step 3: Construct Initial Guesses

The motion primitive graph is searched to produce sequences of motion primitives between the initial and target arcs that are refined to produce initial guesses for the trajectory design problem [31]. Two approaches are used to search the graph. The first approach employs a depth-first search (DFS), consistent with the prior work by Smith and Bosanac, to produce all possible motion primitive sequences with a desired length [31]. However, when the graph becomes larger and more complex, a depth-first search can become computationally expensive and time-consuming. Thus, this paper presents an improvement on the previous search method by using Dijkstra's and Yen's algorithm as an alternative approach to search the graph for longer motion primitive sequences. As demonstrated by Bruchko and Bosanac, Yen's algorithm offers an alternative approach to computing multiple sufficiently distinct paths through a graph [44]. Once generated, the motion primitive sequences are refined to reduce any potential overlap between arcs and minimize the discontinuity between arcs. These refined sequences supply a variety of initial guesses with distinct geometries, flight times, and maneuver requirements.

Dijkstra's algorithm searches the shortest path between two nodes in a weighted graph. Starting from the initial node, the algorithm explores the neighboring nodes, computes the cost to pass through each of them, and saves the node associated with the minimum cost as the second node. This process is repeated for the subsequent nodes until the destination node is reached or all the reachable nodes have been visited. Therefore, the result is the path in the graph that minimizes the edge weights [45]. Accordingly, Dijkstra's algorithm is used to generate the primitive sequence with the globally lowest cumulative edge weight between the initial and target node; this path is initializes the list of motion primitive sequences for further analysis.

Yen's algorithm is used to identify k additional loopless paths within a directed weighted graph. First, multiple subgraphs are constructed by iteratively removing one edge from the initial path at a time from the original graph. Dijkstra's algorithm is then reapplied to identify paths within these subgraphs. These paths are added to the list of motion primitive sequences for further analysis. This process is repeated until the N best or all the possible paths are identified. The paths in this list are then ordered based on the cumulative edge weights. In this paper, the search with Yen's algorithm usually takes a few seconds, while the search with DFS can take a few seconds to up to 45 minutes depending on the graph size and the desired number of paths. Despite its good performance, Yen's algorithm has some limitations including the high computational time for large graphs and the possibility of producing multiple paths with a high similarity. The latter problem can be addressed by only storing paths that are sufficiently dissimilar from the existing paths in the list; this approach has been demonstrated by Bruchko and Bosanac to produce geometrically distinct trajectories from a graph search and this improvement is an avenue of ongoing work [44].

The generated list of motion primitive sequences that connect the initial and target arcs are refined and trimmed to improve their quality prior to corrections. First, the sequences of motion primitives are morphed to reduce the state discontinuity between subsequent arcs. Specifically, the value of q is computed for all possible combinations of primitives or their associated exemplars. The morphed motion primitive sequence is equal to the sequence of arcs with the lowest value of q. Each segment of the morphed primitive sequence is trimmed to remove any overlapping segments. The trimming process is applied to all segments except the target arc through one of the following three methods, selected by the user:

1) Forward trimming is applied to the beginning of an arc to minimize the value of q measured from the final state of the previous arc
2) Backward trimming is applied to the end of an arc to minimize the value of q measured from the initial state of the next arc
3) Joint trimming simultaneously trims the end of one arc and the start of the next arc to minimize the value of q

The trimming method is selected as whichever of the three approaches produces the lowest cumulative value of q. To facilitate an effective corrections process, any segments that do not exceed a specified minimum integration time of 0.01 non-dimensional time units are removed. This refinement and trimming process produces an initial guess for a trajectory.

D. Step 4: Correct And Optimize Initial Guesses

The discontinuous initial guess generated using the motion primitive sequence is corrected using collocation to obtain a continuous trajectory with impulsive maneuvers. This corrections scheme is implemented using constrained, multi-objective, local optimization. Using the approach developed by Smith and Bosanac [31], this optimization problem is formulated to balance retaining the geometry of the initial guess with minimizing the square of the maneuver magnitudes.

Formulating the constrained optimization problem requires the specification of an objective function, equality constraints, and free variables. First, the free variables and constraints are selected as those used to solve the collocation problem as defined in Section II.C. Then, the objective function is defined as

$$J = w_{geo}(\Delta \boldsymbol{r}_{IG-CT})^2 + w_{man} \sum_{i=1}^{n_m} (\Delta v_i)^2 \tag{18}$$

where $\Delta \boldsymbol{r}_{IG-CT}$ is the difference between the position vectors of each collocation node along the initial guess and current guess, and Δv_i is the magnitude of the i-th of n_m impulsive maneuvers along the trajectory. Thus, the first term encourages geometric resemblance between the initial guess and current guess whereas the second term encourages a more energy-efficient use of maneuvers. Note that the choice of minimizing the value of $(\Delta v)^2$ rather than Δv improves the convexity of the problem, thereby making the optimization problem easier to solve [46]. To balance these two competing objectives, w_{geo} and w_{man} are scalar weights that are either set by the user to a fixed value or varied gradually.

To solve the optimization problem, an initial guess for the free variable vector is required along with a solution method. To construct the initial guess for the free variable vector, the refined primitive sequence generated in Step 3 is discretized into an initial mesh of nodes. This step requires specifying the number of arcs within each segment as well as the placement of any maneuvers. In this paper, the arcs are located between apses along the segment. Although there are a variety of options for maneuver placement, from those that are informed by the dynamics to those that rely on operational practices, maneuvers are placed between segments, at apses, and at maxima and minima in curvature function along each segment in this paper. Using this initial guess and maneuver locations, the nonlinear optimization problem is solved using the Interior Point Optimizer (IPOPT) library with the 'mumps' linear solver for a maximum of 1000 iterations with a constraint tolerance of 10^{-12} [47–49]. More details about the corrections process appear in Smith and Bosanac [31].

Continuation is employed to generate an array of trajectories with a varying balance between resembling the original initial guess and minimizing the sum of the square of the maneuver magnitudes. To implement this continuation scheme, the scalar weights in Equation 18 are gradually varied. In the first step, a single solution is generated by solving the optimization problem with $[w_{geo}, w_{man}] = [0.9, 0.1]$ or $[w_{geo}, w_{man}] = [1.0, 0.0]$, depending on the quality of the initial guess. As a result, this first solution is a continuous trajectory that prioritizes resembling the initial guess. Then, this trajectory supplies the initial guess for the next step in the continuation process where the value of w_{geo} is slightly reduced and w_{man} is slightly increased. Solving the optimization problem with these new weights produces a continuous trajectory with lower maneuver magnitudes than the previous trajectory and a slightly larger deviation from the original guess. This process is repeated until $[w_{geo}, w_{man}] = [0.1, 0.9]$. In most cases, the continuation process is performed with 10 steps in the values of w_{geo} and w_{man}, but the number can be increased or decreased as needed based on the sensitivity of correcting the solutions near each initial guess.

IV. Results

The motion primitive approach is used to compute a planar transfer in the Neptune-Triton CR3BP from an initial state that corresponds to a high-energy interplanetary arrival condition to a selected periodic orbit. In this section, the initial state and target orbit are defined. Then, families of fundamental solutions are selected to construct a library of motion primitives and the associated graph reflecting their potential for sequential composability. Once primitive sequences are generated from the graph, the associated initial guesses are used to generate several sets of geometrically distinct transfers.

A. Initial State

The selected initial state for each transfer occurs after the spacecraft's arrival into the Neptunian system following the interplanetary transfer. In this paper, information about a representative state at periapsis relative to Neptune has been provided by Dr. Reza Karimi from the NASA Jet Propulsion Laboratory (JPL) based on an interplanetary trajectory generated during a mission design activity at a prior JPL Planetary Science Summer School [50]. The periapsis relative to Neptune possesses the following characteristics:

- Epoch at periapsis, t_1: October 2, 2045, 11:52:51 UTC
- Periapsis altitude relative to Neptune's surface: 2460.11 km
- Hyperbolic excess velocity, v_∞: 11.5252 km/s
- Declination angle, the angle between the velocity vector and the XY-plane of the Neptune-fixed frame labeled 'IAU_NEPTUNE' in the 'pck00011.tpc' kernel: $\delta = 8.3778°$

This state is propagated backward in time for 3.75 days to generate an initial state that occurs soon after arrival into the Neptune-Triton system, prior to the sensitive location of periapsis, and far enough from Neptune to offer a variety of potential initial maneuver locations. Following this initial state, maneuvers are required to slow the spacecraft down to ensure within the Neptunian system and insertion into a mission orbit to perform scientific measurements.

The selected initial state, transformed to the Neptune-Triton rotating frame, is modified to generate a nearby, planar initial state for use in this paper. The original initial state possesses an inclination of 20.64° relative to the Neptune-Triton plane and a Jacobi constant of 0.950382, well below the Jacobi constants of L_4 and L_5. Propagating this initial state forward in time for 7.5 days in the Neptune-Triton CR3BP produces the arc plotted in red in Fig. 1. To facilitate a planar transfer design problem in this initial demonstration, the z and $\dot{z}$ components of this initial state are set equal to zero and the remaining state components are slightly adjusted to avoid impact with Neptune. This modified, planar initial state is propagated forward in time for 7.5 days in the Neptune-Triton CR3BP, producing the blue path in Fig. 1 with a Jacobi constant of $C_{J,0} = 0.963141$. This blue path is supplied to the motion primitive graph to enable the first maneuver to occur at any location within 7.5 days after the initial state. Designing spatial transfers from the original initial state is an avenue of future work.

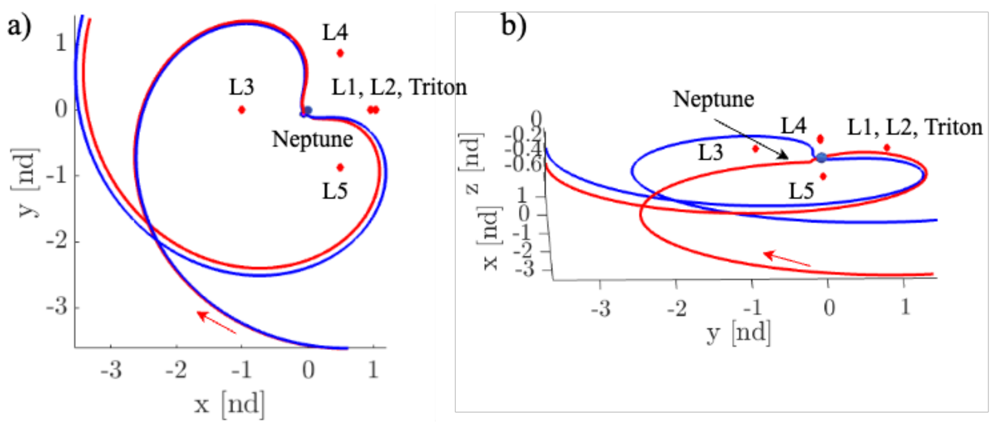

Fig. 1 Trajectories resulting from the original, spatial (red) and modified, planar (blue) initial states in the Neptune-Triton CR3BP, a) projected onto the xy-plane of the Neptune-Triton rotating frame and b) in a 3-dimensional view.

B. Selecting a Target Orbit

As an active and potential ocean world, studying the internal composition of Triton may represent a fundamental goal of a future mission to the Neptune system. Magnetic induction measurement is one proposed approach for identifying subsurface oceans on bodies such as Triton; in this case, it is valuable to take these measurements when Triton crosses Neptune's magnetic field [20]. The requirements associated with performing these measurements influence the selection of a suitable mission orbit. These requirements, as discussed by Cochrane et al., include that spacecraft must perform at least two flybys of Triton at altitudes between 300 and 350 km and at latitudes between ±30° with respect to Triton's equator. These flyby locations should be equally distributed along Triton's orbit such that $\Delta\theta = 2\pi/n_{flybys}$, or with a span of $\Delta\theta = 45°$ between consecutive passages, where θ is the true anomaly along Triton's orbit [20]. Thus, considering 2 flybys per spacecraft's orbit period, these should occur at locations separated by $\Delta\theta = 180°$ or at $b/2$ periods of Triton's orbit, where b is any odd natural number. Given these requirements, candidate mission orbits have been identified as periodic orbits that exist within various well-known exterior, planar resonant families in the Neptune-Triton CR3BP. Among the identified candidates, selecting the target orbit with the lowest Jacobi constant implicitly reduces the change in energy that the maneuvers must achieve along the transfer. Thus, a planar, 3:4 resonant orbit that is prograde in the inertial frame at $C_{J,f} = 1.75598$ is used as the target orbit in this paper because it satisfies the requirements with the lowest value of the Jacobi constant and possesses a similar direction of motion to the initial arrival into the system in the rotating frame. This target orbit is displayed in Fig. 2 in the Neptune-Triton rotating frame.

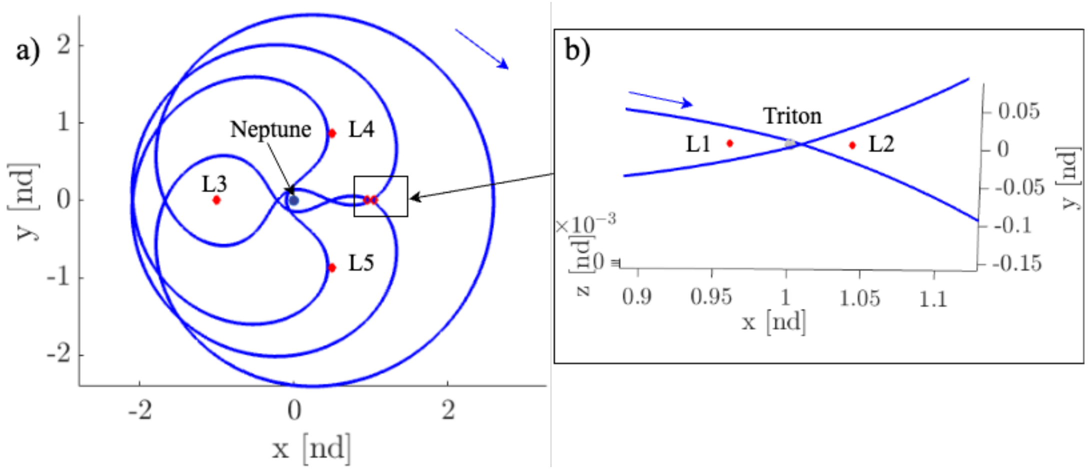

Fig. 2 a) 3:4 resonant orbit in the Neptune-Triton CR3BP selected as the target orbit and b) a zoomed-in view of the trajectory during the closest approaches with Triton.

C. Generating Motion Primitives

Motion primitives are constructed to summarize selected families of periodic orbits and some of their hyperbolic invariant manifolds. The experience of the trajectory designer, as well as an examination of the energy levels and geometry of the trajectory design space are the main considerations used to select the desired families of fundamental solutions. First, recall that the initial state and target orbits possess Jacobi constants of $C_{J,0} = 0.963141$ and $C_{J,f} = 1.75598$, respectively. Accordingly, planar, periodic orbit families and/or invariant manifolds are selected to span a similar range of energy levels. Among the candidate fundamental solutions with C_J within this range, those with a similar direction of motion and/or location within the system to the initial and target orbits are selected as potential candidates. In this paper, the following planar, periodic orbit families and hyperbolic invariant manifolds are summarized via motion primitives:

- L_3 Lyapunov orbit family
- 1:2, 1:3, 1:4, and 1:5 prograde resonant orbit families with periapsis on the $-\hat{x}$-axis
- 2:3, 3:5 and 4:5 prograde resonant orbit families
- 3:4 prograde resonant orbit families with periapsis on the $-\hat{x}$-axis
- 3:1 retrograde resonant orbit families with periapsis on each of the $+\hat{x}$- and $-\hat{x}$-axes
- 4:1 retrograde resonant orbit family
- Stable and unstable invariant manifolds associated with 7 members of the 1:2 prograde resonant orbit family
- Stable and unstable invariant manifolds associated with 6 members of the 1:3 prograde resonant orbit family
- Stable and unstable invariant manifolds associated with 4 members of the 1:4 prograde resonant orbit family
- Stable and unstable invariant manifolds associated with 5 members of the 1:5 prograde resonant orbit family
- Stable invariant manifolds associated with the target 3:4 prograde resonant orbit

In this list, the specification of the periapsis location, measured relative to Neptune, is used to differentiate between two possible families that may exist for each resonance with a specific direction of motion. This periapsis location also influences the stability of the family [24]. The resonant orbits used to generate stable and unstable manifolds also tend to have in-plane stability indices that are close to 2. Accordingly, segments of the stable and unstable manifolds are only stored once they sufficiently depart the vicinity of the resonant orbits.

Motion primitives are computed to summarize the selected periodic orbit families as described in Section III.A. Examples of the generated primitives and the regions of the configuration space spanned by arcs with a similar geometry are displayed in Fig. 3 for a) the 1:3 prograde resonant orbit family and b) the 3:1 retrograde resonant orbit family. In Fig. 3, the left part of each subfigure displays the periodic orbits sampled along the associated family. The right of

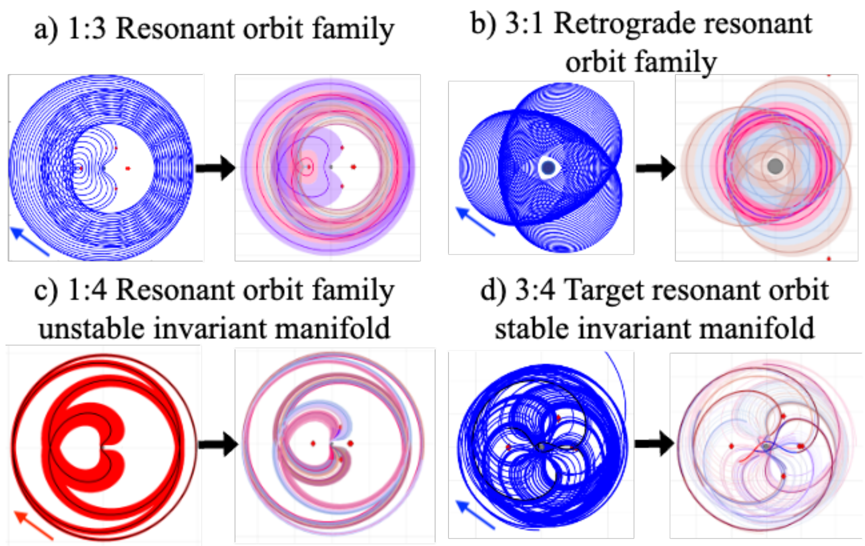

Fig. 3 Motion primitives summarizing the a) 1:3 resonant orbit family, b) 3:1 retrograde resonant orbit family, c) unstable manifolds of the 1:4 resonant orbit family, and d) unstable manifolds of the 3:4 target resonant orbit.

each subfigure, however, displays the computed set of motion primitives (bold) and their associated arcs with a similar geometry (shaded regions). Repeating this process for all families listed in the previous paragraph, Figure 4 summarizes the values of the Jacobi constant of the primitives (black diamonds) and their associated arcs (uniquely colored regions) along each family. On the vertical axis, each family is labeled and a small graphical representation of the primitives is included to aid interpretation. Within each family, each cluster of trajectories is assigned a unique color. Although these colors are repeated across families for visual clarity, they are independent groupings. On the horizontal axis of Fig. 4, the values of the Jacobi constant for the initial state and the target orbit are also highlighted.

Motion primitives are also computed to summarize the stable and unstable manifolds associated with selected periodic orbits. In this paper, stable and unstable manifolds are only generated from selected unstable periodic orbits with Jacobi constants between $C_{J,0} = 0.963141$ and $C_{J,f} = 1.75598$. Table 1 lists the Jacobi constants of the selected periodic orbits within each family that are used to generate stable and unstable manifolds. Trajectories that are generated along these manifolds are first split into segments defined by the maxima and minima in curvature. These segments are then sampled with 10 nodes equally spaced in arclength and clustered using the feature vector defined in Eq. 16. Two examples of the generated primitives and the regions of the configuration space spanned by arcs with a similar geometry are displayed in Fig. 3 for c) the unstable manifold of a set of 1:4 resonant orbits and d) the stable manifold of the target 3:4 resonant orbit.

Table 1 Periodic orbits used to generate stable and unstable manifolds

Orbit Family	Jacobi Constant of Selected Periodic Orbits
1:2 prograde resonant orbit family	$C_J = [1.50, 1.56, 1.61, 1.65, 1.70, 1.75, 1.81]$
1:3 prograde resonant orbit family	$C_J = [1.22, 1.30, 1.35, 1.40, 1.45, 1.51]$
1:4 prograde resonant orbit family	$C_J = [1.15, 1.17, 1.20, 1.25]$
1:5 prograde resonant orbit family	$C_J = [1.09, 1.10, 1.12, 1.13, 1.15]$
3:4 prograde resonant orbit family	$C_J = 1.75598$

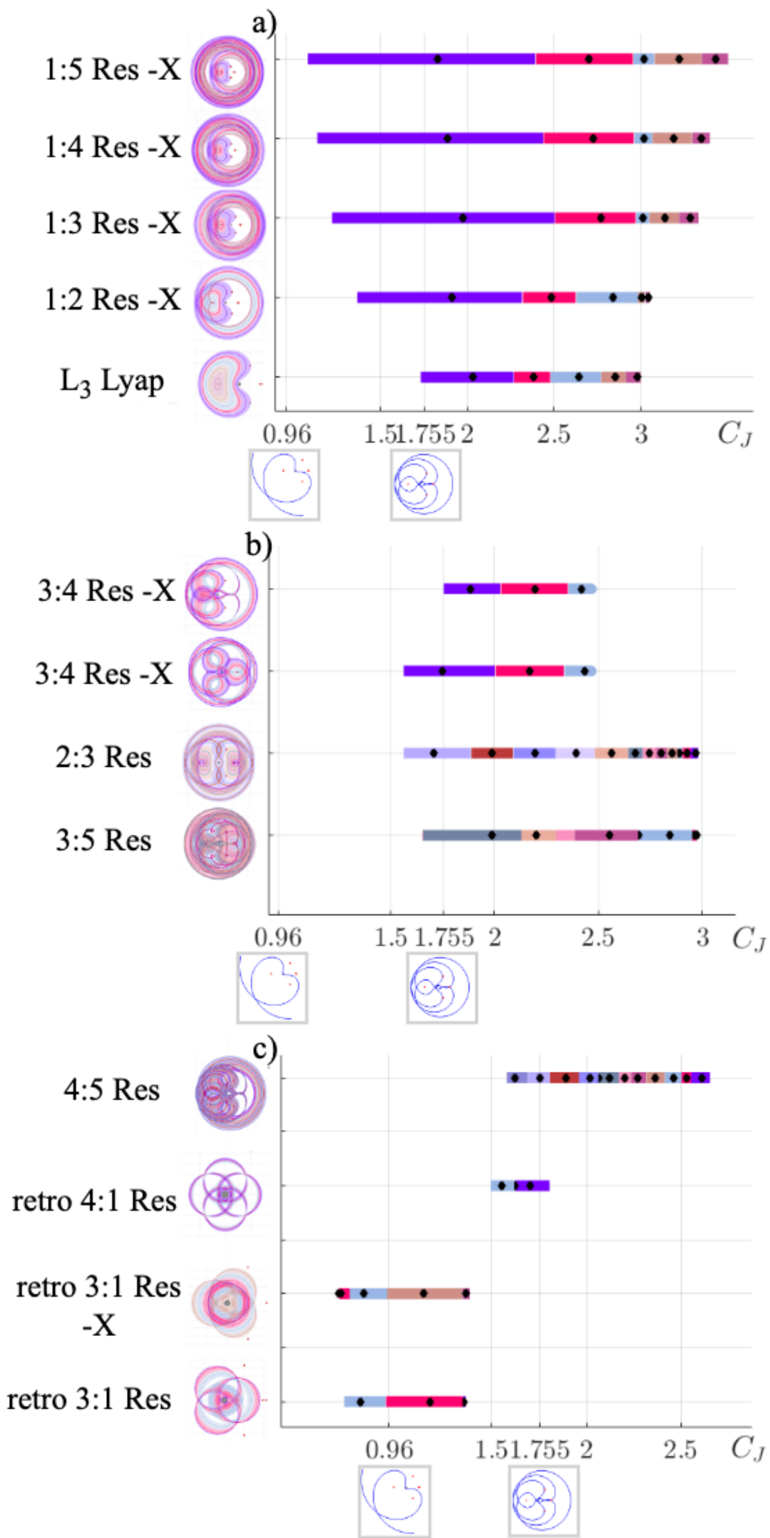

Fig. 4 Values of the Jacobi constant spanned by the motion primitive (black diamonds) for each family and arcs that possess a similar geometry (shaded regions).

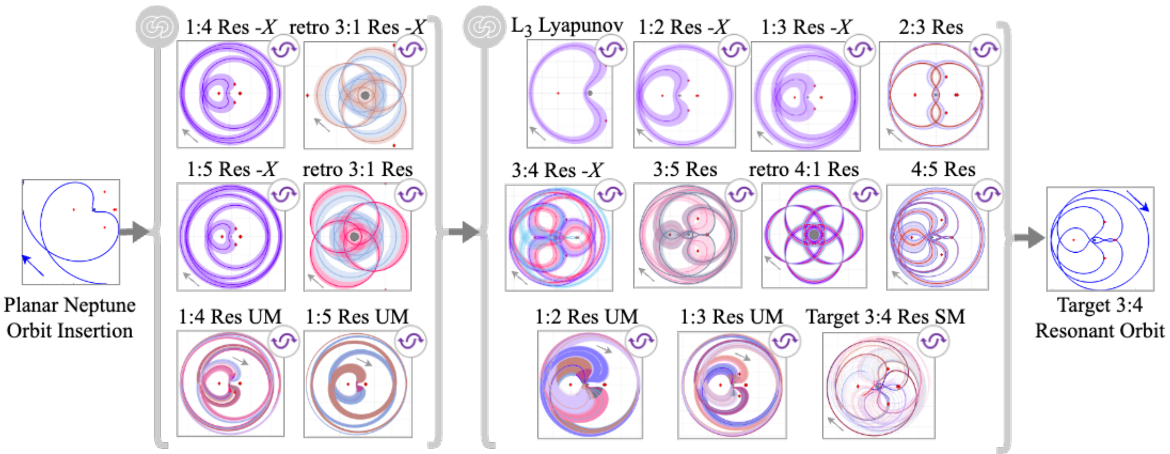

Fig. 5 High-level representation of the motion primitive graph to construct a transfer from a planar NOI to the target 3:4 resonant orbit. In the name tags above each family, SM or UM stands for stable or unstable manifold, retro for retrograde, and $-X$ for periapsis on the $-\hat{x}$-axis.

D. Constructing a Motion Primitive Graph

Selected motion primitives and their associated exemplars are used to form a motion primitive graph. Using Fig. 4 as a reference, only motion primitives and their associated exemplars that encompass Jacobi constants between $C_{J,0} = 0.963141$ and $C_{J,f} = 1.75598$ are included in the motion primitive graph. This graph is structured as displayed in Fig. 5 to include 4 connected, high-level components, from left to right: an arc associated with the initial state, a group of primitives characterized by lower values of the Jacobi constant, a group with the remaining primitives with Jacobi constants close to the value of $C_{J,f}$, and the target orbit. Each of the subgraphs associated with a single type of fundamental solution is internally connected, as indicated by purple circular arrows in Fig. 5; for these edges, the value of q is calculated using the second approach in Section III.B. Each of these subgraphs within the same high-level component of Fig. 5 are connected to each other via bi-directional connections, indicated by the gray chain symbol at the top left of each component. Then, subgraphs within each high-level component are connected to subgraphs in the subsequent high-level component via uni-directional edges, indicated by dark gray arrows. When connecting primitives from distinct subgraphs, the value of q is computed using the fourth approach in III.B. For all edges throughout the graph, $\alpha_{pos} = 5$ and $\alpha_{vel} = 1$ are used in Equation 17. These values are selected empirically and may be adjusted as appropriate to identify alternative motion primitive sequences.

E. Initial Guesses

The motion primitive graph is searched using Dijkstra's and Yen's algorithms as well as the depth-first-search algorithm as described in Section III.C. First, Yen's algorithm is used to search for the 1,000 lowest cost primitive sequences with a maximum path length of 50 primitives. However, all these primitive sequences were composed of no fewer than 10 primitives. To generate shorter sequences of five primitives, the DFS is also applied. These primitive sequences are then morphed and trimmed. A selection of the resulting initial guesses is displayed in Fig. 6: a), b), and c) are primitive sequences obtained using Dijkstra's and Yen's algorithms, whereas d) and e) are obtained from the application of DFS. In each subfigure, each segment derived from the associated motion primitive sequence is uniquely colored. These initial guesses possess various geometries, flight times, and changes in the Jacobi constant between segments, enabling rapid generation of distinct types of trajectories that connect the initial state to the target orbit.

F. Corrected Transfers

The initial guesses are corrected to produce a nearby continuous trajectory that prioritizes resembling the initial guess. First, each primitive is discretized into segments between each apsis with respect to Neptune. Then, each segment is discretized into 15 arcs that are equally spaced in time. These arcs and segments govern the construction of the initial mesh of nodes described in Section III.B. To facilitate an effective corrections process, the maneuvers are located at apoapses and periapses with respect to Neptune, at curvature extrema, and between segments. Placing the

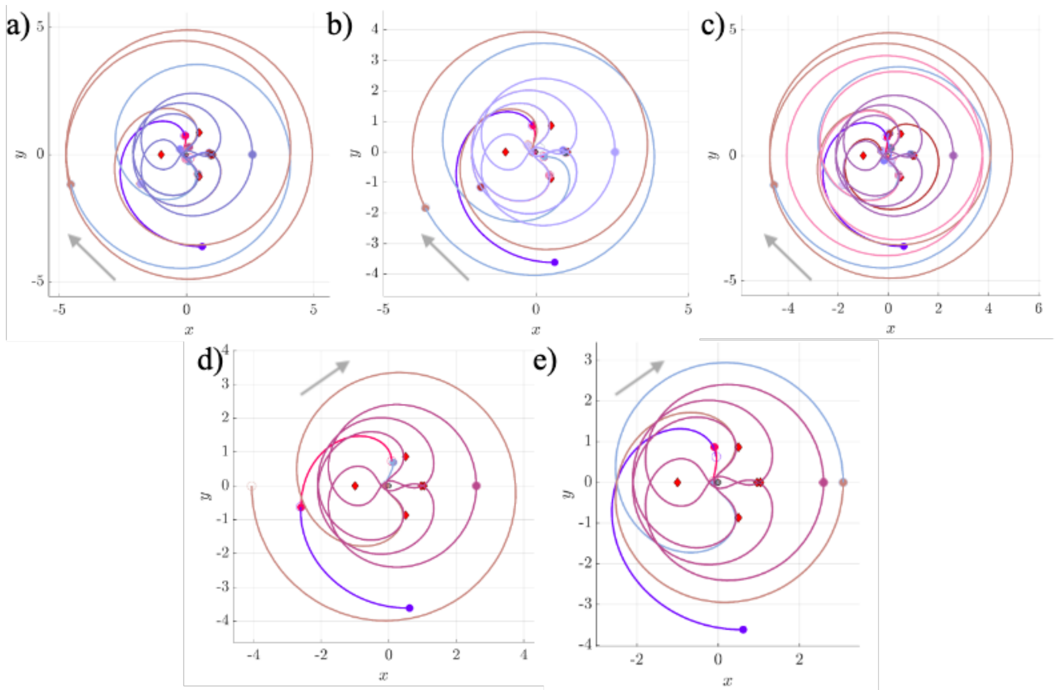

Fig. 6 Selected initial guesses generated by searching the motion primitive graph.

impulsive maneuvers between segments corresponds to locations of discontinuities in the initial guess. On the other hand, maneuvers at apses and extrema in curvature decrease the sensitivity of corrections and result in a lower total Δv. As described in Section III.D, the weights for the objective function at this first step are set to $[w_{geo}, w_{man}] = [0.9, 0.1]$ to prioritize continuous trajectories that resemble the initial guess. The optimization problem described in Section III.D is then solved with each of the initial guesses in Fig. 6 to produce continuous transfers. Figure 7 displays the time of flight (TOF) and total Δv of the trajectories obtained from the initial guesses in Fig. 6 b), d) and e) because the initial guess in Fig. 6 a) and c) resulted in an excessively high total Δv at this initial step.

The corrected trajectories are then input to the continuation scheme described in section III.D to produce geometrically similar transfers with a significantly lower total maneuver requirement. Fig 8 displays the properties of the transfers generated during each continuation step for the initial guesses in Fig 7 a) and c). The leftmost subfigures display the transfers, the center subfigures display the maneuver requirements as a function of TOF, and the rightmost subfigures

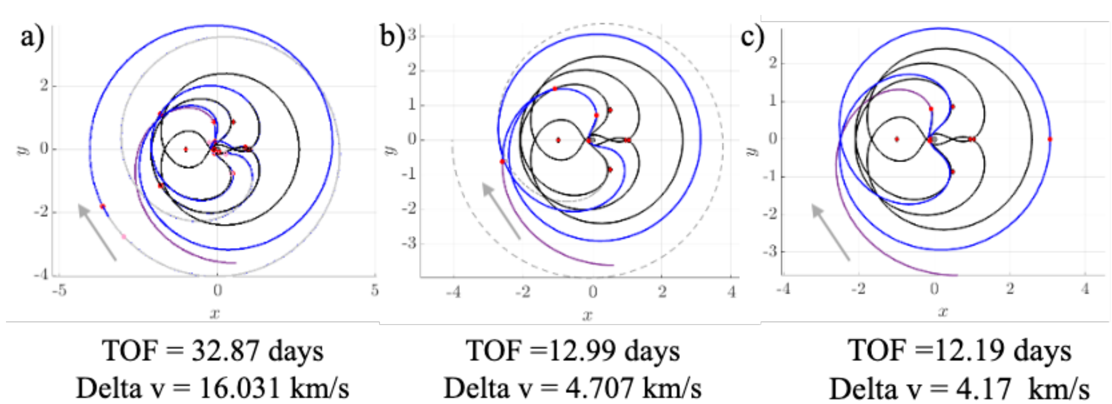

Fig. 7 Trajectories initially corrected to prioritize closely resembling three of the initial guesses in Fig. 6.

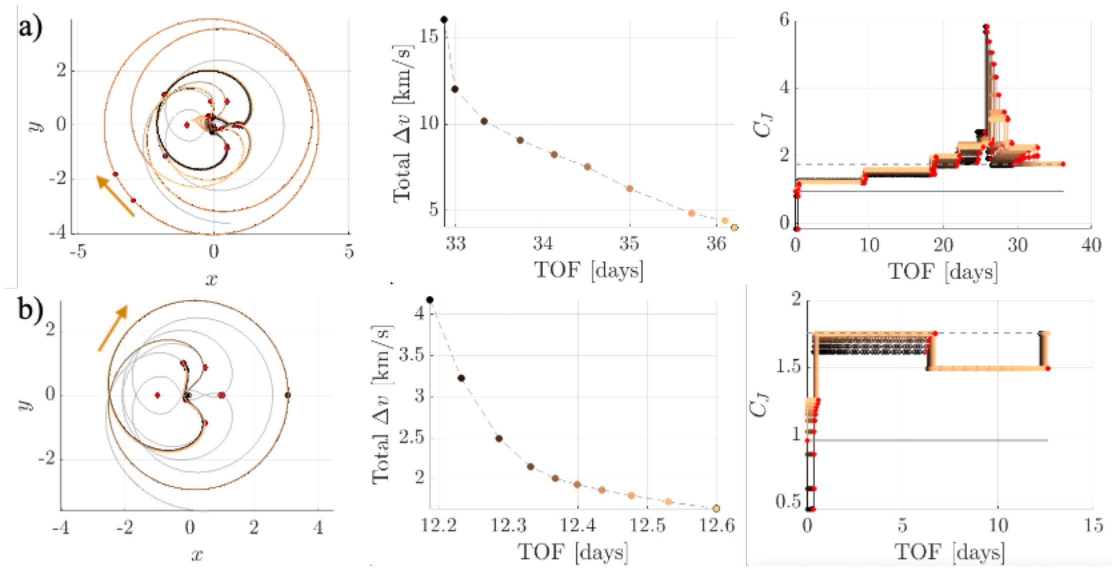

Fig. 8 Summary of the transfers generated by applying continuation to the initial guesses in a) Fig. 7b) and b) Fig. 7 e). In each row, the colors vary from black to gold as the optimization weights vary from $[w_{geo}, w_{man}] = [0.9, 0.1]$ **to** $[w_{geo}, w_{man}] = [0.1, 0.9]$**.**

display the variation in the Jacobi constant along each trajectory as a function of time. In each component of the figure, the transfers are colored from black to gold as the optimization weights vary from $[w_{geo}, w_{man}] = [0.9, 0.1]$ to $[w_{geo}, w_{man}] = [0.1, 0.9]$ and the maneuver locations are denoted with red markers. Following continuation, the transfer geometry in Fig. 8 a) includes a trajectory with a TOF of 36.21 days and a total Δv of 4.05 km/s. The transfer geometry in Fig. 8 b), however, includes a trajectory with a TOF of 12.60 days and with Δv = 1.64 km/s. Applying continuation to the trajectory in Fig 7 b) produces a transfer with a TOF of 12.93 days and with Δv = 1.87 km/s. The three transfers generated after continuation to possess the lowest total maneuver requirements are displayed in Fig 9 along with their TOF and required Δv. Together, these transfers offer an initial demonstration of the capability for a motion primitive approach to recover geometrically distinct trajectories that deliver the spacecraft from the high-energy interplanetary arrival condition to the selected target orbit in the Neptune-Triton CR3BP.

Given the high-energy arrival conditions to the system and the Jacobi constant of the target orbit, a significant total Δv is expected. As a comparison, consider a study for the Uranus Orbiter and Probe mission design by Simon et al. [51]. Although this study involved a different target system, interplanetary trajectories to either Uranus or Neptune typically result in a high arrival energy. In their study, they estimate an available Δv = 2.708 km/s for a Uranus orbiter and probe, encompassing any maneuvers that occur after launch [51]. To insert into an elliptical orbit about Uranus in

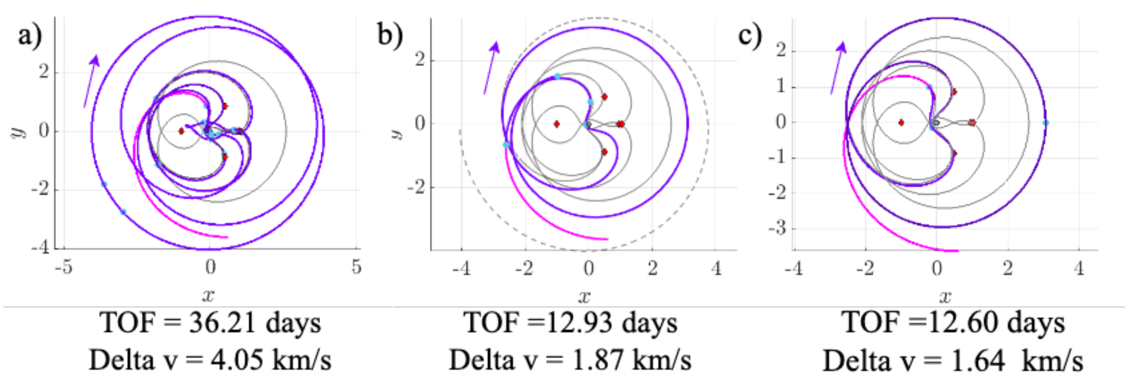

Fig. 9 Three transfers with the lowest maneuver requirements from the initial state to the selected 3:4 resonant orbit in the Neptune-Triton CR3BP.

resonance with Titania, 1.0867 km/s of this available Δv is employed. As a high-level comparison to the results in this paper, the two trajectories with the lowest total maneuver requirements in Fig. 9 require Δv = 1.64 km/s and Δv = 1.87 km/s after arrival into the Neptunian system. These values are higher than but comparable to the magnitude of the orbit insertion maneuver in the Uranus orbiter and probe study.

To expand the results presented in this paper, several avenues of work may be fruitful. First, it is possible that further continuation or alternative maneuver placement strategies may result in a further reduction of the total maneuver requirements for the transfer geometries presented in this paper. Ongoing work also includes expansion of the motion primitive graph, generation of additional transfer geometries, and improvement of the search algorithms to support generating a wider array of transfers. Future studies will also apply this motion primitive approach to designing spatial trajectories to a wider variety of target orbits in a higher-fidelity model of the Neptune-Triton system.

V. Conclusions

This paper uses a motion primitive approach to design planar trajectories that connect a high-energy interplanetary arrival condition to a mission orbit in the Neptune-Triton CR3BP. The transfer targets a planar 3 : 4 resonant orbit that is selected based on a notional scientific goal of performing magnetometric induction measurements at Triton. First, a motion primitive library is generated to summarize a set of periodic orbit families and their invariant manifolds. The motion primitives are then connected in a graph structure to reflect their potential for connectivity. The graph is searched using Dijkstra's and Yen's algorithms to find long primitive sequences that produce the lowest cost solutions as well as a depth-first search to obtain shorter primitive sequences. The sequences of motion primitives generated by these algorithms are then trimmed and morphed to create a discontinuous initial guess connecting the initial state to the target 3 : 4 resonant orbit. The initial guesses presented in this paper exhibit distinct geometries and flight times. These initial guesses are corrected and optimized. From the three types of transfers generated in this paper, there are transfers with flight times as low as 12.60 days and total maneuver requirements as low as 1.64 km/s.

Acknowledgments

This work was completed at the University of Colorado Boulder with funding from the Strategic University Research Partnership program at the Jet Propulsion Laboratory, California Institute of Technology, under a contract with the National Aeronautics and Space Administration (80NM0018D0004). The authors thank Dr. Thomas Smith for answering technical questions. Additionally, the authors thank Dr. Reza Karimi for providing information on the initial state and valuable discussions. The first author is also grateful for many valuable discussions with JPL scientists and engineers during the summer of 2023.

References

[1] National Academies of Sciences, Engineering, and Medicine, "NASA 2023 Decadal Survey," Technical report, National Academies Press, Washington, D.C., 2023.

[2] Swenson, B., "Neptune atmospheric probe mission," *Guidance, Navigation and Control Conference*, American Institute of Aeronautics and Astronautics, 1992. https://doi.org/10.2514/6.1992-4371.

[3] Masters, A., Achilleos, N., Agnor, C., Campagnola, S., Charnoz, S., Christophe, B., Coates, A., Fletcher, L., Jones, G., Lamy, L., Marzari, F., Nettelmann, N., Ruiz, J., Ambrosi, R., Andre, N., Bhardwaj, A., Fortney, J., Hansen, C., Helled, R., Moragas-Klostermeyer, G., Orton, G., Ray, L., Reynaud, S., Sergis, N., Srama, R., and Volwerk, M., "Neptune and Triton: Essential pieces of the Solar System puzzle," *Planetary and Space Science*, Vol. 104, 2014, pp. 108–121. https://doi.org/10.1016/j.pss.2014.05.008.

[4] Rymer, A. M., Runyon, K. D., Clyde, B., Núñez, J. I., Nikoukar, R., Soderlund, K. M., Sayanagi, K., Hofstadter, M., Quick, L. C., Stern, S. A., Becker, T., Hedman, M., Cohen, I., Crary, F., Fortney, J. J., Vertesi, J., Hansen, C., de Pater, I., Paty, C., Spilker, T., Stallard, T., Hospodarsky, G. B., Smith, H. T., Wakeford, H., Moran, S. E., Annex, A., Schenk, P., Ozimek, M., Arrieta, J., McNutt, R. L., Masters, A., Simon, A. A., Ensor, S., Apland, C. T., Bruzzi, J., Patthoff, D. A., Scott, C., Campo, C., Krupiarz, C., Cochrane, C. J., Gantz, C., Rodriguez, D., Gallagher, D., Hurley, D., Crowley, D., Abel, E., Provornikova, E., Turtle, E. P., Clark, G., Wilkes, J., Hunt, J., Roberts, J. H., Rehm, J., Murray, K., Wolfarth, L., Fletcher, L. N., Spilker, L., Martin, E. S., Parisi, M., Norkus, M., Izenberg, N., Stough, R., Vervack, R. J., Mandt, K., Stevenson, K. B., Kijewski, S., Cheng, W., Feldman, J. D., Allen, G., Prabhu, D., Dutta, S., Young, C., and Williams, J., "Neptune Odyssey: A Flagship Concept for the Exploration of the Neptune–Triton System," *Planet. Sci. J.*, Vol. 2, No. 5, 2021, p. 184. https://doi.org/10.3847/PSJ/abf654.

[5] Vallado, D. A., *Fundamentals of Astrodynamics and Applications, Fifth Edition*, Microcosm Press, New York, 2022.

[6] Marley, M. e. a., “Planetary Science Decadal Survey JPL Rapid Mission Architecture Neptune-Triton-KBO Study Final Report,” Technical report, NASA Jet Propulsion Laboratory, Pasadena, CA, 2010.

[7] Melman, J., Orlando, G., Safipour, E., Mooij, E., and Noomen, R., “Trajectory Optimization for a Mission to Neptune and Triton,” *AIAA/AAS Astrodynamics Specialist Conference and Exhibit*, 2007, p. 7366.

[8] Koon, W., Lo, M., Marsden, J., and Ross, S., *Dynamical Systems, The Three-Body Problem, and Space Mission Design*, Springer, New York, USA, 2011.

[9] Smith, T. R., and Bosanac, N., “Constructing Motion Primitive Sets to Summarize Periodic Orbit Families and Hyperbolic Invariant Manifolds in a Multi-Body System,” *Celestial Mechanics and Dynamical Astronomy*, Vol. 134, No. 1, 2022, p. 7. https://doi.org/10.1007/s10569-022-10063-x.

[10] Smith, T. R., and Bosanac, N., “A Motion Primitive Approach To Trajectory Design In A Multi-Body System,” *AAS/AIAA Astrodynamics Specialists Conference*, 2022.

[11] Wolek, A., and Woolsey, C. A., *Model-Based Path Planning*, Springer International Publishing, Cham, 2017, pp. 183–206. https://doi.org/10.1007/978-3-319-55372-6_9.

[12] Frazzoli, E., “Robust Hybrid Control for Autonomous Vehicle Motion Planning,” PhD Dissertation, Massachusetts Institute of Technology, Cambridge, MA, 2001.

[13] Paranjape, A. A., Meier, K. C., Shi, X., Chung, S. J., and Hutchinson, S., “Motion Primitives and 3D Path Planning for Fast Flight Through a Forest,” *Int. J. Robot. Res.*, Vol. 34, No. 3, 2015, pp. 357–377. DOI: https://doi.org/10.1177/0278364914558017.

[14] Wang, B., Gong, J., Zhang, R., and Chen, H., “Learning to Segment and Represent Motion Primitives from Driving Data for Motion Planning Applications,” *21st International Conference on Intelligent Transportation Systems*, Maui, HI, 2018, pp. 1408–1414. DOI: https://doi.org/10.1109/ITSC.2018.8569913.

[15] Reng, L., Moeslund, T. B., and Granum, E., “Finding Motion Primitives in Human Body Gestures,” *Gesture in Human-Computer Interaction and Simulation: 6th International Gesture Workshop*, Berder Island, France, 2005, pp. 133–144. DOI: https://doi.org/10.1007/11678816_16.

[16] Majumdar, A., and Tedrake, R., “Funnel Libraries for Real-Time Robust Feedback Motion Planning,” *Int. J. Robot. Res.*, Vol. 36, No. 8, 2017, pp. 947–982. DOI: https://doi.org/10.1177/0278364917712421.

[17] Kulic, D., Takano, W., and Nakamura, Y., “Incremental Learning, Clustering and Hierarchy Formation of Whole Body Motion Patterns using Adaptive Hidden Markov Chains,” *The International Journal of Robotics Research*, Vol. 27, No. 7, 2008, pp. 761–784.

[18] Dermy, O., Paraschos, A., Ewerton, M., Peters, J., Charpillet, F., and Ivaldi, S., “Prediction of Intention during Interaction with iCub with Probabilistic Movement Primitives,” *Frontiers in Robotics and AI*, Vol. 4, 2017.

[19] Clever, D., Harant, M., Koch, H., Mombaur, K., and Endres, D., “A Novel Approach for the Generation of Complex Humanoid Walking Sequences Based on a Combination of Optimal Control and Learning of Movement Primitives,” *Robotics and Autonomous Systems*, Vol. 83, 2016, pp. 287–298.

[20] Cochrane, C. J., Persinger, R. R., Vance, S. D., Midkiff, E. L., Castillo-Rogez, J., Luspay-Kuti, A., Liuzzo, L., Paty, C., Mitchell, K. L., and Prockter, L. M., “Single- and Multi-Pass Magnetometric Subsurface Ocean Detection and Characterization in Icy Worlds Using Principal Component Analysis (PCA): Application to Triton,” *Earth and Space Science*, Vol. 9, No. 2, 2022. https://doi.org/https://doi.org/10.1029/2021EA002034.

[21] Szebehely, V., *Theory of Orbits: The Restricted Problem of Three Bodies*, Academic Press, London, 1967.

[22] National Aeronautics and Space Administration (NASA), “Neptunian Satellite Fact Sheet,” , 2023. URL https://nssdc.gsfc.nasa.gov/planetary/factsheet/neptuniansatfact.html, accessed: 11-13-2023.

[23] NASA Navigation and Ancillary Information Facility (NAIF), “NASA Navigation and Ancillary Information Facility (NAIF) Generic Kernels,” , 2023. URL https://naif.jpl.nasa.gov/pub/naif/generic_kernels/.

[24] Murray, C. D., and Dermott, S. F., *Solar system dynamics*, Cambridge university press, 1999.

[25] Vaquero Escribano, T. M., "Spacecraft transfer trajectory design exploiting resonant orbits in multi-body environments," Ph.D. thesis, Purdue University, West Lafayette, Indiana, 2013.

[26] Howell, K. C., "Three-Dimensional Periodic Halo Orbits," *Celestial Mechanics*, Vol. 32, No. 1, 1984, p. 53.

[27] Conway, B. A., *Spacecraft Trajectory Optimization*, Cambridge University Press, New York, 2010.

[28] Topputo, F., and Zhang, C., "Survey of Direct Transcription for Low-Thrust Space Trajectory Optimization with Applications," *Abstract and Applied Analysis*, 2014, p. 851720. https://doi.org/https://doi.org/10.1155/2014/851720, publisher: Hindawi Publishing Corporation.

[29] Betts, J. T., "Survey of Numerical Methods for Trajectory Optimization," *Journal of Guidance, Control, and Dynamics*, Vol. 21, No. 2, 1998, pp. 193–207. https://doi.org/10.2514/2.4231.

[30] Grebow, D. J., and Pavlak, T. A., "MCOLL: Monte Collocation Trajectory Design Tool," AAS/AIAA Astrodynamics Specialist Conference, Stevenson, Washington, August 20-24, 2017, 2017. URL https://hdl.handle.net/2014/46415.

[31] Smith, T. R., and Bosanac, N., "Motion Primitive Approach to Spacecraft Trajectory Design in a Multi-body System," *The Journal of the Astronautical Sciences*, Vol. 70, No. 34, 2023. https://doi.org/10.1007/s40295-023-00395-7.

[32] Kelly, M., "An Introduction to Trajectory Optimization: How to Do Your Own Direct Collocation," *SIAM Review*, Vol. 59, No. 4, 2017, pp. 849–904. https://doi.org/10.1137/16M1062569.

[33] Pritchett, R. E., "Strategies for Low-Thrust Transfer Design Based on Direct Collocation Techniques," Thesis, Purdue University Graduate School, 2020. https://doi.org/10.25394/PGS.12739775.v1.

[34] Ozimek, M., Grebow, D., and Howell, K., "A Collocation Approach for Computing Solar Sail Lunar Pole-Sitter Orbits," *Open Aerospace Engineering Journal*, Vol. 3, 2010, pp. 65–75. https://doi.org/10.2174/1874146001003010065.

[35] Williams, P., "Hermite-Legendre-Gauss-Lobatto Direct Transcription in Trajectory Optimization," *Journal of Guidance, Control, and Dynamics*, Vol. 32, No. 4, 2009, pp. 1392–1395. https://doi.org/10.2514/1.42731.

[36] De Boor, C., "Good Approximation by Splines with Variable Knots. II," *Proceedings of the Conference on the Numerical Solution of Differential Equations*, Dundee, Scotland, 1973.

[37] Russell, R., and Christiansen, J., "Adaptive Mesh Selection Strategies for Solving Boundary Value Problems," *SIAM Journal on Numerical Analysis*, Vol. 15, No. 1, 1978, pp. 59–80.

[38] Patrikalakis, N. M., Maekawa, T., and Cho, W., *Shape Interrogation for Computer Aided Design and Manufacturing*, Springer, New York, NY, 2009.

[39] Bosanac, N., "Data-Driven Summary of Natural Spacecraft Trajectories in the Earth-Moon System," AAS/AIAA Astrodynamics Specialist Conference, Big Sky, Montana, August 13-17, 2023.

[40] Spear, R. L., and Bosanac, N., "Data-Driven Categorization of Spacecraft Motion with Uncertainty in the Earth-Moon System," AAS/AIAA Astrodynamics Specialist Conference, Big Sky, Montana, August 13-17, 2023.

[41] Mark Van der Laan, K. P., and Bryan, J., "A new partitioning around medoids algorithm," *Journal of Statistical Computation and Simulation*, Vol. 73, No. 8, 2003, pp. 575–584. https://doi.org/10.1080/0094965031000136012.

[42] Han, J., Kamber, M., and Pei, J., *Data Mining: Concepts and Techniques*, Morgan Kaufmann Publishers, Waltham, 2012.

[43] LaValle, S. M., *Planning Algorithms*, Cambridge University Press, Cambridge, 2006.

[44] Bruchko, K. L., and Bosanac, N., "Rapid Trajectory Design In Multi-Body Systems Using Sampling-Based Kinodynamic Planning," AAS/AIAA Astrodynamics Specialist Conference, Big Sky, Montana, August 13-17, 2023.

[45] Dijkstra, E. W., "A note on two problems in connexion with graphs," *Edsger Wybe Dijkstra: His Life, Work, and Legacy*, 2022, pp. 287–290.

[46] Parrish, N. L., and Scheeres, D. J., "Low-Thrust Trajectory Optimization with Simplified SQP Algorithm," *AAS/AIAA Astrodynamics Specialist Conference*, 2017. URL https://ntrs.nasa.gov/citations/20170007868.

[47] Wächter, A., and Biegler, L. T., "On the Implementation of a Primal-Dual Interior Point Filter Line Search Algorithm for Large-Scale Nonlinear Programming," *Mathematical Programming*, Vol. 106, No. 1, 2006, pp. 25–57. https://doi.org/10.1007/s10107-004-0559-y.

[48] Amestoy, P. R., Duff, I. S., L'Excellent, J.-Y., and Koster, J., "A fully asynchronous multifrontal solver using distributed dynamic scheduling," *SIAM Journal on Matrix Analysis and Applications (SIMAX)*, Vol. 23, No. 1, 2001, pp. 15–41. https://doi.org/10.1137/S0895479899358194.

[49] Bertolazzi, E., "mexIPOPT," , 2023. URL https://github.com/ebertolazzi/mexIPOPT/releases/tag/1.1.6, gitHub. Retrieved November 12, 2023.

[50] "Private communication with Dr. Reza Karimi," , July 2023. NASA Jet Propulsion Laboratory.

[51] Simon, A., Nimmo, F., and Anderson, R. C., "Journey to an Ice Giant System: Uranus Orbiter and Probe," Planetary Mission Concept for the 2023–2032 Planetary Science Decadal Survey, June 7 2021. Retrieved May 1, 2022.